Results in Physics 8 (2018) 473–480

Contents lists available at ScienceDirect

Results in Physics

journal homepage: www.journals.elsevier.com/results-in-physics

Non-Darcy flow of water-based carbon nanotubes with nonlinear radiation and heat generation/absorption

T. Hayat [a,b], Siraj Ullah [a,*], M. Ijaz Khan [a], A. Alsaedi [b], Q.M. Zaigham Zia [c]

[a] Department of Mathematics, Quaid-I-Azam University 45320, 44000, Pakistan

[b] Nonlinear Analysis and Applied Mathematics (NAAM) Research Group, Department of Mathematics, Faculty of Science, King Abdulaziz University, P.O. Box 80257, Jeddah 21589, Saudi Arabia

[c] Department of Mathematics, COMSATS Institute of Information Technology Islamabad, Campus Park Road, Tarlai Kalan, Islamabad, Pakistan

ARTICLE INFO

Article history:
Received 17 November 2017
Received in revised form 12 December 2017
Accepted 13 December 2017
Available online 20 December 2017

Keywords:
Porous medium
Heat generation/absorption
SWCNTs and MWCNTs
Nonlinear radiation

ABSTRACT

Here modeling and computations are presented to introduce the novel concept of Darcy-Forchheimer three-dimensional flow of water-based carbon nanotubes with nonlinear thermal radiation and heat generation/absorption. Bidirectional stretching surface induces the flow. Darcy's law is commonly replace by Forchheimer relation. Xue model is implemented for nonliquid transport mechanism. Nonlinear formulation based upon conservation laws of mass, momentum and energy is first modeled and then solved by optimal homotopy analysis technique. Optimal estimations of auxiliary variables are obtained. Importance of influential variables on the velocity and thermal fields is interpreted graphically. Moreover velocity and temperature gradients are discussed and analyzed. Physical interpretation of influential variables is examined.

Introduction

A carbon nanotube (CNTs) is a tube shaped material, allotropes of carbon with a cylindrical nanostructure. These carbon molecules in cylindrical shape have exceptional characteristics, which are beneficial for nanotechnology, optics, electronics and other fields of materials science and engineering. Owing to the material's excellent strength and stiffness the cylindrical nanotubes are established with length-to-diameter ratio up to 132,000,000 remarkably higher when compared with other material. Carbon nanotubes have extensive applications in different fields for example in tissue engineering, prostheses, genomics, pharmacogenomics, drug delivery, surgery and general medicine etc. Carbon nanotubes can be categorized into two subclasses. These depend on structure of material, namely single wall carbon nanotubes (SMCNTs) and multi wall carbon nanotubes (MWCNTs). Thermal conductivity enhancement through nanotube suspension is examined by Choi et al. [1]. They considered oil based nanoliquids comprising carbon nanotubes and found that nanotubes yield remarkable thermal conductivity enhancement. A model based on Maxwell theory valid for carbon nanotubes (CNTs) characteristics transport is presented by Xue [2]. Non-Fourier heat flux and unsteady chemically reactive flow through SWCNTs and MWCNTs is investigated by Hayat et al. [3]. They considered Xue model for the effective thermal conductivity of nanoliquid. They found that Nusselt number is enhanced for large thermal relaxation and curvature parameters. MHD flow of carbon water nanomaterial by a stretchable disk with Marangoni convection and Rosseland approximation is explored by Mahanthesh et al. [4]. They used Runge-Kutta method via shooting technique to find out the computational results of nonlinear expressions. Their results illustrated that heat transfer rate increases for higher Marangoni number and nanoparticles volume fraction. However it declines for magnetic variable. MHD slip flow with convective heat transport in presence of SWCNTs and MWCNTs is analyzed by Haq et al. [5]. Recently few meaningful attempts for flows with SWCNTs and MWCNTs have been presented these studies [6–10].

Flow through porous space have extensive applications in various fields like petroleum engineering, industries and geothermal operations. Flow regime in porous space is commonly characterized by a dimensionless number (Reynolds number). Darcy's law is valid to describe flow in porous space at low flow rates i.e., $(Re < 1)$ (when flow rate and pressure gradient have linear relationship). This law predicts that viscous forces dominate over inertial forces in porous space. Mostly flow in porous space is described by Darcy's law, this law is not adequate for high flow rates. For higher flow rates the Forchheimer relation is used. Infact

* Corresponding author.
E-mail address: sirajsafi151@gmail.com (S. Ullah).

https://doi.org/10.1016/j.rinp.2017.12.035
2211-3797/© 2017 Published by Elsevier B.V.

Nomenclature

u, v, w	velocity components	T_w	surface temperature
C_p	specific heat	T_∞	ambient temperature
F_I	Forchheimer parameter	κ_{fh}	Forchheimer permeability
ν_{nf}	kinematic viscosity	μ_{nf}	dynamic viscosity
σ^*	Stefan Boltzman constant	ρ_{nf}	density of nanofluid
$(\rho c_p)_{nf}$	heat capacity	k_{nf}	Effective thermal conductivity
q_w	heat flux	Nr	radiation parameter
λ	heat generation/absorption parameter	k^*	mean absorption coefficient
μ_f	dynamic viscosity	ρ_f	density of fluid
Pr	Prandtl number	Re_x	Reynold number
ω	porosity parameter	θ_w	temperature ratio variable
ϕ	volume fraction of nanomaterial	Nu_x	Nusselt number
C_{fx}	skin friction coefficient	q_r	radiative flux
τ_w	shear stress	k	thermal conductivity parameter
nf	nanofluid		

Forchheimer [11] introduced a new nonlinear contribution of velocity which is called Forchheimer term. Hayat et al. [12] investigated Darcy Forchheimer flow of ferromagnetic second grade fluid over a stretchable sheet. Some recent investigations about Darcy-Forchheimer flow can be seen in the studies [13–20].

In view of fast development of human society, numerous energy problems emerge for example environmental pollution and storage of global energy. Engineers and scientists are engaged in modeling new resources for sustainable energy. Solar energy is best source of renewable energy which offers a solution to this issue. Heat transport subject to Rosseland approximation has many applications in engineering, physics, nuclear plants and space technology, aerodynamic rockets, solar power technology, gas cooled nuclear reactors, counting combustion, furnace design, nuclear reactor protection and photo chemical reactors etc. Cortell [21] initially examined radiative flow over a stretchable surface. Sheikholeslami et al. [22] explored MHD flow of nanomaterial in subject to thermal radiation. Reddy et al. [23] studied impact of nonlinear radiation MHD flow of ferroliquids with temperature dependent viscosity. Few modern investigations on this topic can be mentioned in Refs. [24–30].

The purpose of present attempt is to model three-dimensional flow subject to SWCNTs and MWCNTs, Darcy-Forchheimer relation for porous space is considerd. Heat transfer process is explored subject to nonlinear thermal radiation and heat generation/absorption. Outcomes of SWCNT and MWCNT with water as base fluid are achieved and compared. Xue model [2] of nanomaterial is employed. The resulting nonlinear expressions are solved by Optimal homotopy analysis method (OHAM) [31]. Heat transfer rate and surface drag forces are computed and discussed.

Problem statement

Three-dimensional Darcy-Forchhiemer flow of water and carbon nanotubes are considered. Both single (SWCNTs) and multiple (MWCNTs) walls carbon nanotubes are studied. Flow is due to bidirectional stretchable surface. Heat transport process is examined through nonlinear thermal radiation and heat absorption/generation. Xue [2] model for nanoliquid transport is implemented. In cartesian coordinates system, the flow equations are governed by

$$\frac{\partial u}{\partial x}+\frac{\partial v}{\partial y}+\frac{\partial w}{\partial z}=0, \tag{1}$$

$$u\frac{\partial u}{\partial x}+v\frac{\partial u}{\partial y}+w\frac{\partial u}{\partial z}=\nu_{nf}\frac{\partial^2 u}{\partial z^2}-\frac{\nu_{nf}}{\kappa_{fh}}u-F_0u^2, \tag{2}$$

$$u\frac{\partial v}{\partial x}+v\frac{\partial v}{\partial y}+w\frac{\partial v}{\partial z}=\nu_{nf}\frac{\partial^2 v}{\partial z^2}-\frac{\nu_{nf}}{\kappa_{fh}}v-F_0v^2, \tag{3}$$

$$(\rho c_p)_{nf}\left(u\frac{\partial T}{\partial x}+v\frac{\partial T}{\partial y}+w\frac{\partial T}{\partial z}\right)=k_{nf}\frac{\partial^2 T}{\partial z^2}-\frac{\partial q_r}{\partial z}+Q_0(T-T_\infty), \tag{4}$$

with

$$u=U_w(x)=ax,\quad v=V_w(y)=by,\quad w=0,\quad T=T_w,\quad \text{at } z=0$$
$$u=0,\quad v=0,\quad T\to T_\infty,\quad \text{at } z\to\infty. \tag{5}$$

The theoretical model for nanoliquid transport proposed by Xue [2] gives:

$$\left.\begin{array}{c}\mu_{nf}=\frac{\mu_f}{(1-\phi)^{2.5}},\ \nu_{nf}=\frac{\mu_{nf}}{\rho_{nf}},\ \rho_{nf}=\rho_f(1-\phi)+\rho_s\phi,\\ (\rho c_p)_{nf}=(\rho c_p)_f(1-\phi)+(\rho c_p)_s\phi,\ \frac{k_{nf}}{k_f}=\frac{k_s+2k_f-2\phi(k_f-k_s)}{k_s+2k_f+2\phi(k_f-k_s)}.\end{array}\right\} \tag{6}$$

The radiative heat flux in terms of Rosseland approximation is [26]:

$$q_r=-\frac{4\sigma^*}{3k^*}\frac{\partial T^4}{\partial r}=-\frac{16\sigma^*}{3k^*}T^3\frac{\partial T}{\partial r}. \tag{7}$$

In above expression k^* represents the mean absorption coefficient and σ^* the Stefan-Boltzman constant.

Considering

$$\left.\begin{array}{c}u=axf'(\eta),\ v=ayg'(\eta),\ w=-\sqrt{a\nu_f}(f(\eta)+g(\eta))\\ \theta=\frac{T-T_\infty}{T_w-T_\infty},\ \eta=\sqrt{\frac{a}{\nu_f}}z\end{array}\right\} \tag{8}$$

Eq. (1) is verified and Eqs. (2)–(5) take the form

$$\frac{1}{(1-\phi)^{2.5}\left(1-\phi+\frac{\rho_{CNT}}{\rho_f}\phi\right)}(f'''-\omega f')+f''(f+g)-(1+F_I)f'^2=0, \tag{9}$$

$$\frac{1}{(1-\phi)^{2.5}\left(1-\phi+\frac{\rho_{CNT}}{\rho_f}\phi\right)}(g'''-\omega g')+g''(f+g)-(1+F_I)g'^2=0, \tag{10}$$

$$\left.\begin{array}{l}\frac{1}{\left(1-\phi+\frac{(\rho c_p)_{CNT}}{(\rho c_p)_f}\phi\right)}\left[\frac{k_{nf}}{k_f}\theta''+\lambda\,\mathrm{Pr}\,\theta+Nr(\theta(\theta_w-1)+1)^2\right.\\ \left.\times\left\{\begin{array}{c}3\theta'^2(\theta_w-1)\\ +\theta''(\theta(\theta_w-1)+1)\end{array}\right\}\right]+\mathrm{Pr}\,\theta'(f+g)=0,\end{array}\right\} \tag{11}$$

$$\left.\begin{array}{c} f(0)=0,\ f'(0)=1,\ f'(\infty)=0,\ g(0)=0,\ g'(0)=\alpha, \\ g'(\infty)=0,\ \theta(0)=0,\ \theta(\infty)=1. \end{array}\right\} \quad (12)$$

Here $\omega\left(=\frac{\nu_f}{a\kappa}\right)$ represents the porosity variable, $Pr\left(=\frac{(\mu c_p)_f}{k_f}\right)$ the Prandtl number, $\lambda\left(=\frac{Q_0}{a(\rho c_p)_f}\right)$ the heat generation/absorption variable, $F_I\left(=\frac{C_b}{\sqrt{\kappa_{fh}}}\right)$ the Forchhiemer parameter, $Nr\left(=\frac{16\sigma^* T_\infty^3}{3k^* k_f}\right)$ the radiation variable and $\theta_w\left(=\frac{T_w}{T_\infty}\right)$ the dimensionless temperature ratio variable.

Quantities of physical interest

Skin friction coefficients

Mathematically we have

$$C_{fx}=\frac{2\tau_{w_x}}{\rho_f U_w^2},\quad C_{fy}=\frac{2\tau_{w_y}}{\rho_f U_w^2}, \quad (13)$$

where

$$\tau_{w_x}=\mu_{nf}\left(\frac{\partial u}{\partial z}\right)\Big|_{z=0},\quad \tau_{w_y}=\mu_{nf}\left(\frac{\partial v}{\partial z}\right)\Big|_{z=0}. \quad (14)$$

Inserting Eq. (14) in Eq. (13) one has

$$\left.\begin{array}{l} C_{fx}\,\mathrm{Re}_x^{0.5}=\frac{2f''(0)}{(1-\phi)^{2.5}}, \\ C_{fy}\,\mathrm{Re}_y^{0.5}=\frac{2g''(0)}{\alpha^{\frac{2}{3}}(1-\phi)^{2.5}}. \end{array}\right\} \quad (15)$$

Nusselt number

It is defined as

$$Nu_x=\frac{xq_w}{k_f(T_w-T_\infty)}, \quad (16)$$

where

$$q_w=-k_{nf}\left(\frac{\partial T}{\partial z}\right)\Big|_{r=R}+(q_r)_w. \quad (17)$$

Putting Eq. (17) in Eq. (16) we have

$$Nu_x\,\mathrm{Re}_x^{-0.5}=-\left(\frac{k_{nf}}{k_f}+Nr(\theta(0)(\theta_w-1)+1)^3\right)\theta'(0). \quad (18)$$

In above expressions τ_{w_x} and τ_{wy} represent shear stresses in x- and y-directions, q_w the heat flux and Re_x and Re_y the local Reynolds numbers.

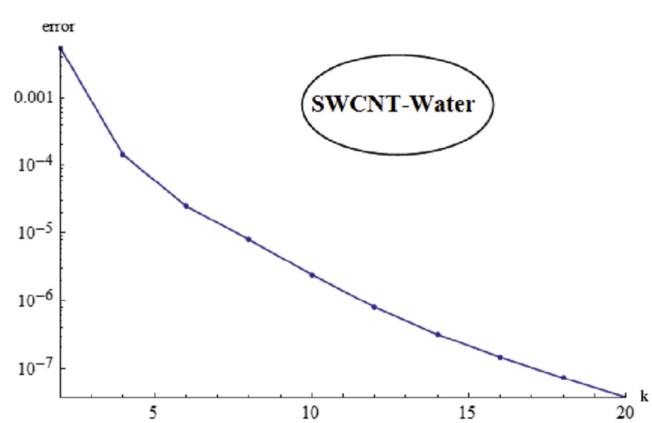

Fig. 1. SWCNTs residual error plots.

OHAM solutions

Initial guesses and operators for the desired solutions are

$$f_0=1-e^{-\eta},\quad g_0=\alpha(1-e^{-\eta}),\quad \theta_0=e^{-\eta}, \quad (19)$$

$$L_f=\frac{d^3f}{d\eta^3}-\frac{df}{d\eta},\quad L_g=\frac{d^3g}{d\eta^3}-\frac{dg}{d\eta},\quad L_\theta=\frac{d^2\theta}{d\eta^2}-\theta. \quad (20)$$

The non-zero auxiliary variables $\hbar_f$, $\hbar_g$ and $\hbar_\theta$ in homotopy solutions indicate the convergence region. To get the optimal estimations of $\hbar_f$, $\hbar_g$ and $\hbar_\theta$ we have utilized the concept given by Liao [31]. The average squared residual errors of the kth order approximation is as follow:

$$\varepsilon_k^f=\frac{1}{N+1}\sum_{i=0}^{N}\left[N_f\left(\sum_{j=0}^{k}(f_j),\sum_{j=0}^{k}(g_j)\right)_{\eta=i\delta\eta}\right]^2, \quad (21)$$

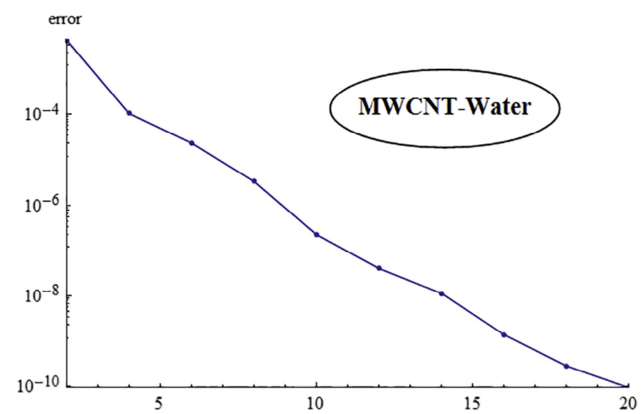

Fig. 2. MWCNTs residual error plots.

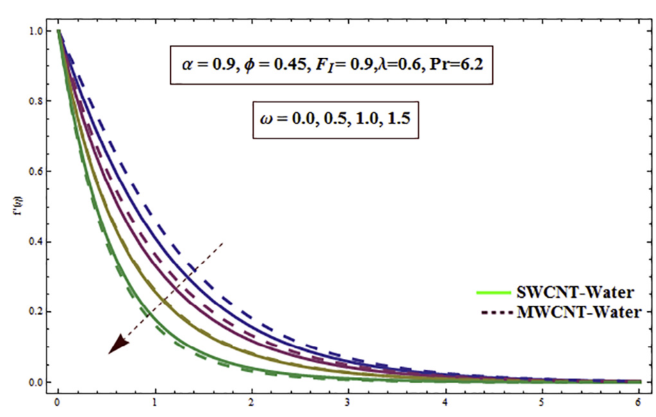

Fig. 3. $f'(\eta)$ via ω.

Table 1
Thermophysical properties for water and SWCNTs and MWCNTs.

Physical properties	Base fluid	Nanoparticles	
	Water	SWCNT	MWCNT
ρ (kg/m^3)	997	2600	1600
c_p (j/kg K)	4179	425	796
k (w/mK)	0.613	6600	3000

Table 2
Estimations of average square residual errors for *SWCNTs* when $\omega = 0.4$, $\phi = 0.1$ and $\lambda = 0.1$.

k	ε_k^f	ε_k^g	ε_k^θ
2	3.32008×10^{-4}	2.76555×10^{-7}	5.16469×10^{-3}
6	8.95163×10^{-6}	2.08492×10^{-9}	1.6136×10^{-5}
10	9.94229×10^{-7}	2.06756×10^{-10}	1.43437×10^{-6}
16	8.31798×10^{-8}	1.72592×10^{-11}	6.22315×10^{-8}
24	5.72362×10^{-9}	1.18649×10^{-12}	4.76692×10^{-9}
30	9.72581×10^{-10}	2.01331×10^{-13}	8.03829×10^{-10}

Table 3
Estimations of average square residual errors for *MWCNTs* when $\omega = 0.4$, $\phi = 0.1$ and $\lambda = 0.1$.

k	ε_k^f	ε_k^g	ε_k^θ
2	8.10583×10^{5}	8.97036×10^{-9}	4.22733×10^{-3}
6	2.80161×10^{-7}	6.45576×10^{-11}	2.38942×10^{-5}
10	3.81951×10^{-9}	8.11443×10^{-13}	2.20259×10^{-7}
16	1.3476×10^{-11}	2.82062×10^{-15}	1.39151×10^{-9}
24	1.34658×10^{-14}	2.81155×10^{-18}	1.87558×10^{-12}
30	9.54607×10^{-17}	1.98982×10^{-20}	2.21502×10^{-14}

$$\overset{g}{\varepsilon}_k = \frac{1}{N+1}\sum_{i=0}^{N}\left[N_g\left(\sum_{j=0}^{k}(f_j), \sum_{j=0}^{k}(g_j)\right)_{\eta=i\delta\eta}\right]^2, \tag{22}$$

$$\overset{\theta}{\varepsilon}_k = \frac{1}{N+1}\sum_{i=0}\left[N_\theta\left(\sum_{j=0}^{k}(f_j), \sum_{j=0}^{k}(g_j), \sum_{j=0}^{k}(\theta_j)\right)_{\eta=i\delta\eta}\right]^2. \tag{23}$$

Total residual error is [31]:

$$\overset{t}{\varepsilon}_k = \overset{f}{\varepsilon}_k + \overset{g}{\varepsilon}_k + \overset{\theta}{\varepsilon}_k. \tag{24}$$

Here $\overset{t}{\varepsilon}_k$ signifies total residual error. The values of convergence control variables for momentum and energy expressions are $h_f = -0.861563$, $h_g = -0.679111$ and $h_\theta = -0.19295$ and $h_f = -0.751529$, $h_g = -0.687246$ and $h_\theta = -0.19914$ for both the cases i.e., (SWCNTs and MWCNTs). The total averaged squared residual error for both SWCNTs and MWCNTs are $\overset{t}{\varepsilon}_k = 5.49697 \times 10^{-3}$ and $\overset{t}{\varepsilon}_k = 4.30848 \times 10^{-3}$ respectively. Figs. 1 and 2 represent average square residual errors for SWCNTs and MWCNTs.

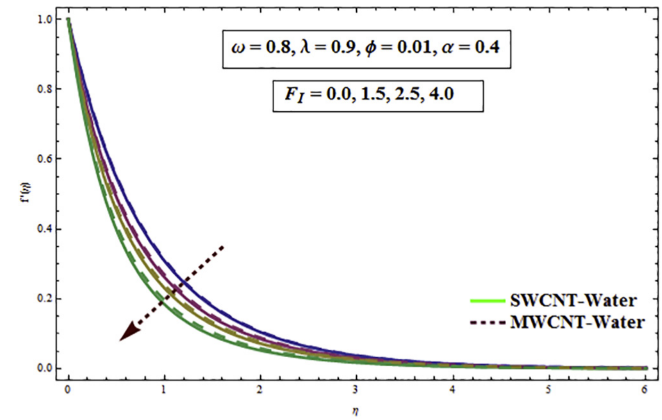

Fig. 4. $f'(\eta)$ via F_I.

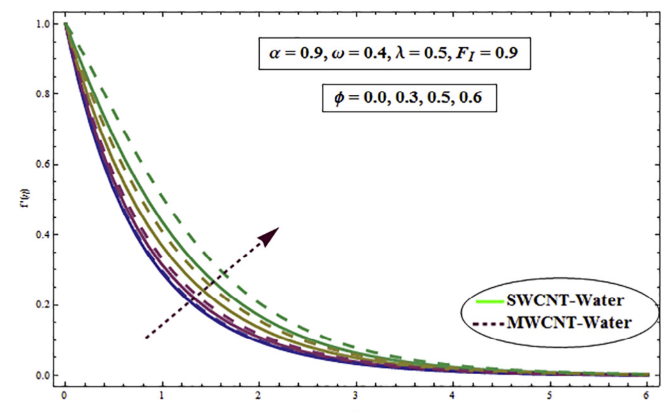

Fig. 5. $f'(\eta)$ via ϕ.

Discussion

This section highlights influences of various physical variables like heat generation/absorption parameter (λ), volume fraction (ϕ), porosity parameter (ω), non-uniform inertia coefficient (F_I), temperature ratio parameter (θ_w) and radiation parameter (Nr) on velocities ($f'(\eta), g'(\eta)$) and temperature ($\theta(\eta)$) for both SWCNTs and MWCNTs. Table 1 characterizes the thermophysical properties of continuous phase base fluid and SWCNTs and MWCNTs. Tables 2 and 3 provide total square residual error for both (*SWCNTs*) and (*MWCNTs*) respectively for distinct order of approximations. Here error decays for higher order of approximations. Table 4 shows

Table 4
Numerical values of ($Cf_x\,Re_x^{0.5}$) for various parameters.

ϕ	ω	F_I	α	$-Cf_x\,Re_x^{0.5}$		$-Cf_y\,Re_y^{0.5}$	
				SWCNTs	*MWCNTs*	*SWCNTs*	*MWCNTs*
0.1	0.3	0.5	0.4	2.90211	2.86991	1.1399	1.16566
0.2				3.81395	3.71753	1.59567	1.67281
0.3				5.14122	4.90268	2.37541	2.56624
	0.1			2.80485	2.76345	1.21771	1.25083
	0.3			2.90211	2.86991	1.1399	1.16566
	0.5			2.99937	2.97637	1.062099	1.08049
		0.1		2.77197	2.73978	1.20237	1.22812
		0.3		2.83704	2.80484	1.17113	1.19689
		0.6		2.93464	2.90245	1.12428	1.15004
			0.2	2.88042	2.84822	0.624173	0.637052
			0.4	2.90211	2.86991	1.1399	1.16566
			0.6	2.9238	2.8916	1.54718	1.58582

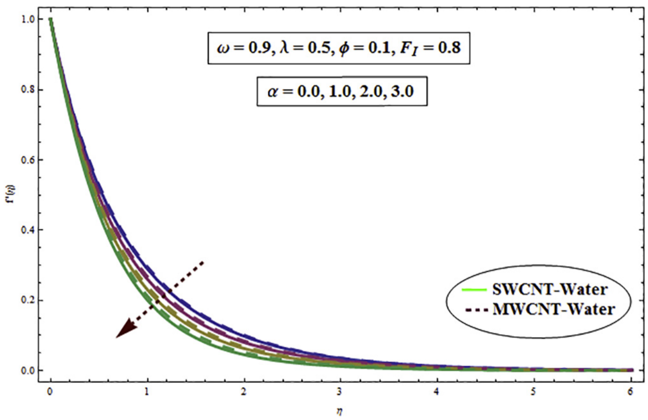

Fig. 6. $f'(\eta)$ via α.

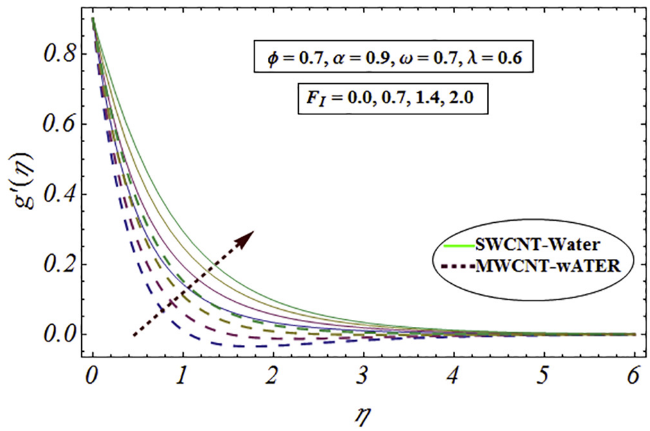

Fig. 9. $g'(\eta)$ via F_I.

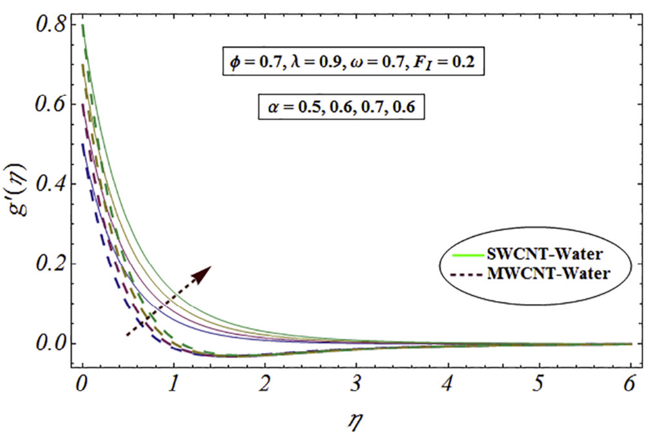

Fig. 7. $g'(\eta)$ via α.

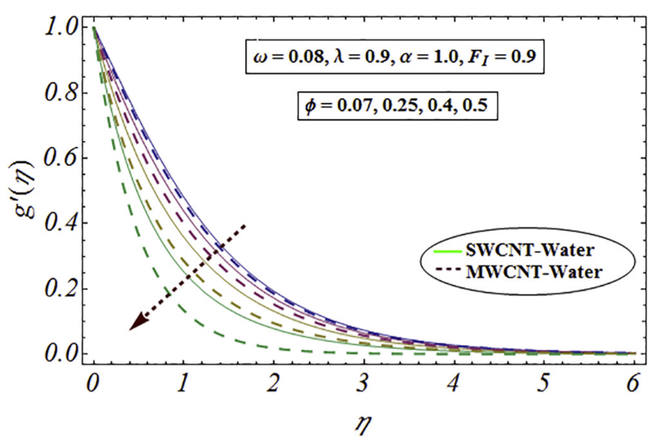

Fig. 10. $g'(\eta)$ via ϕ.

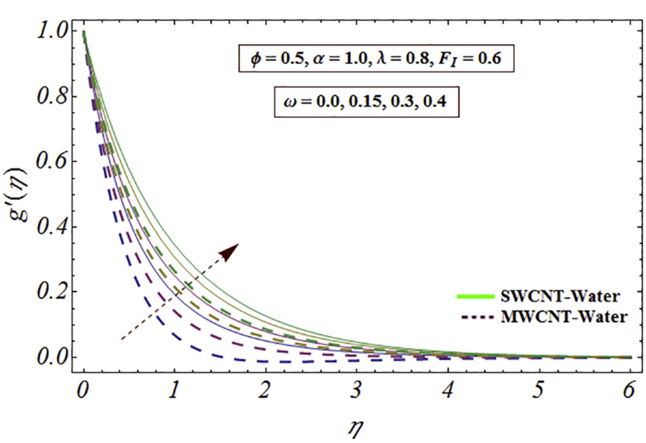

Fig. 8. $g'(\eta)$ via ω.

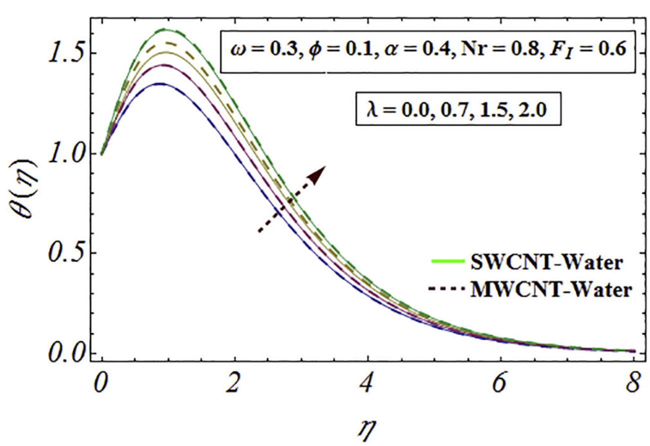

Fig. 11. $\theta(\eta)$ via λ (*heat source case*).

numerical results of surface drag force (skin friction coefficient) for different physical variables. From Table 4 it is found that surface drag force decreases for larger nanoparticle volume fraction and porosity parameter. However opposite behavior is noticed for larger Forchhiemer number. Impact of (ω) on $(f'(\eta))$ is shown in Fig. 3. It is noted that with the enhancement of (ω) the velocity declines for both SWCNTs and MWCNTs. Fig. 4 is sketched to investigate velocity profile for values of Forchhiemer parameter. Here velocity field decays for larger Forchhiemer parameter. Physically for larger Forchhiemer parameter the inertial force enhances and therefore velocity of fluid decays. Nanoparticle volume fraction (ϕ) impact on velocity $(f'(\eta))$ is depicted in Fig. 5. It is examined that velocity and associated layer thickness are enhanced for both SWCNTs and MWCNTs. Further velocity of fluid particle dominant in case of MWCNTs when compared with SWCNTs. Figs. 6 and 7 demonstrate that how the velocity distribution varies by (α).

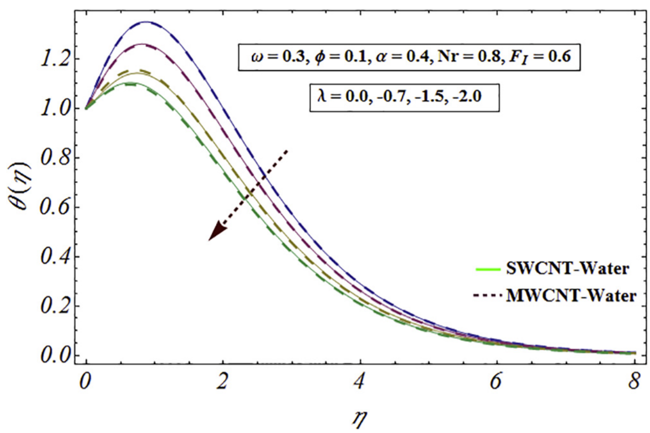

Fig. 12. $\theta(\eta)$ via λ (*heat sink case*).

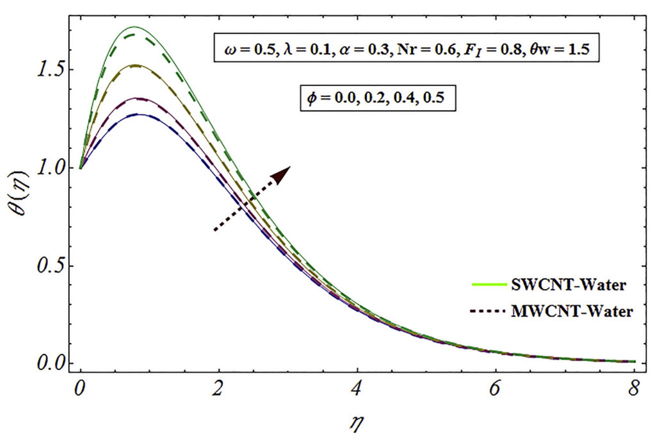

Fig. 13. $\theta(\eta)$ via ϕ.

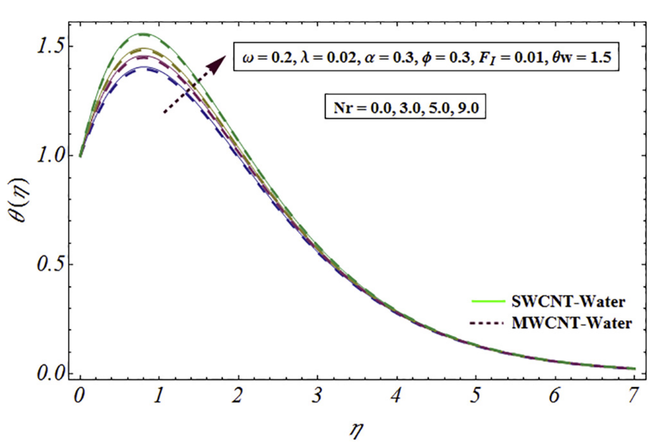

Fig. 14. $\theta(\eta)$ via *Nr*.

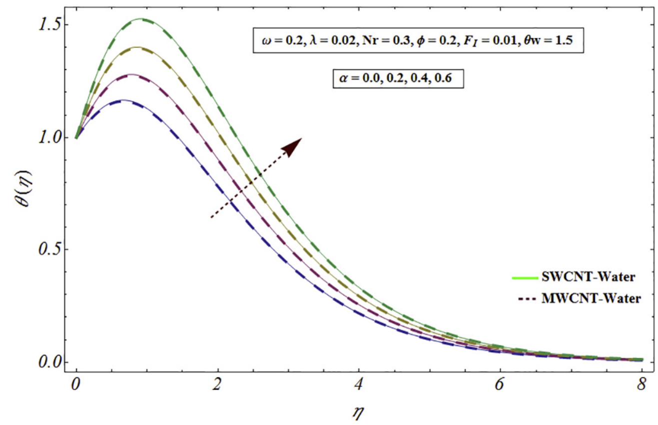

Fig. 15. $\theta(\eta)$ via α.

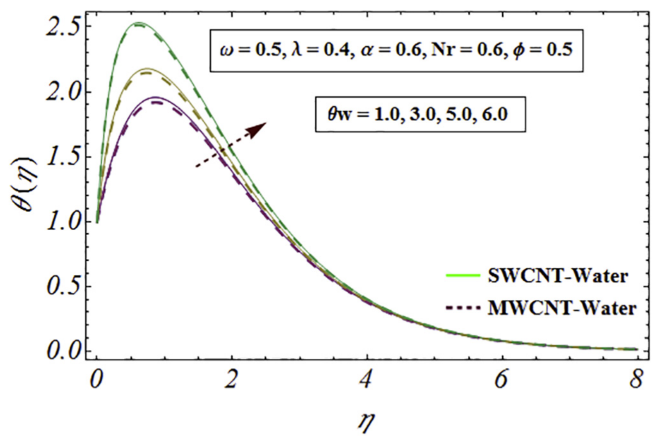

Fig. 16. $\theta(\eta)$ via θ_w.

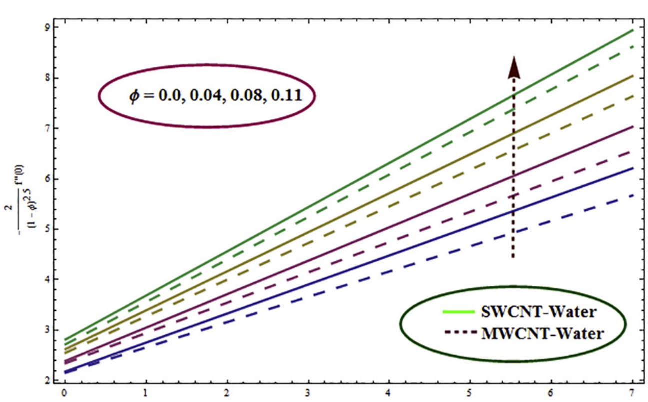

Fig. 17. $Cf_x\, Re_x^{0.5}$ via ϕ and ω.

Velocity and associated layer thickness in x-direction decayed via (α) for both SWCNTs and MWCNTs. Reverse behavior is noticed in y-direction for both SWCNTs and MWCNTs (see Fig. 7). Fig. 8 declares porosity variable effects on velocity field $g'(\eta)$. Here velocity field increases for higher estimation of porosity variable for both SWCNTs and MWCNTs. Fig. 9 is drawn to interpret impact of (F_I) on velocity ($g'(\eta)$). Here ($g'(\eta)$) is increasing function of (F_I). Physically higher estimation of (F_I) constitutes larger inertial forces which oppose the flow motion and therefore velocity field decays. Influence of nanoparticle volume fraction (ϕ) on ($g'(\eta)$) is shown in Fig. 10. Through Fig. 10 the velocity decays when nanoparticle volume fraction (ϕ) increases for both SWCNTs and MWCNTs. It is also observed that velocity dominantes in case of MWCNTs when compared with SWCNTs. Consequences of heat

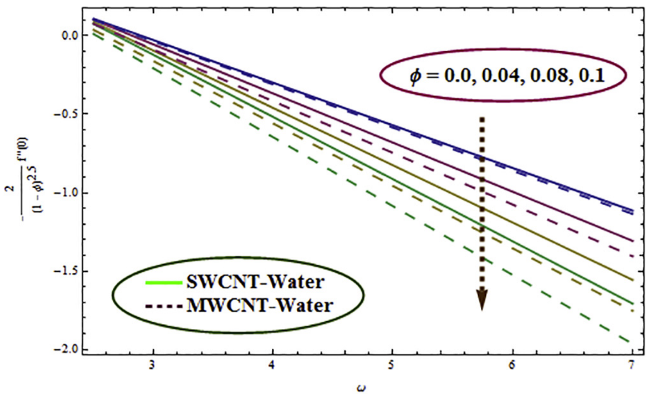

Fig. 18. $Cf_y\,\mathrm{Re}_y^{0.5}$ via ϕ and ω.

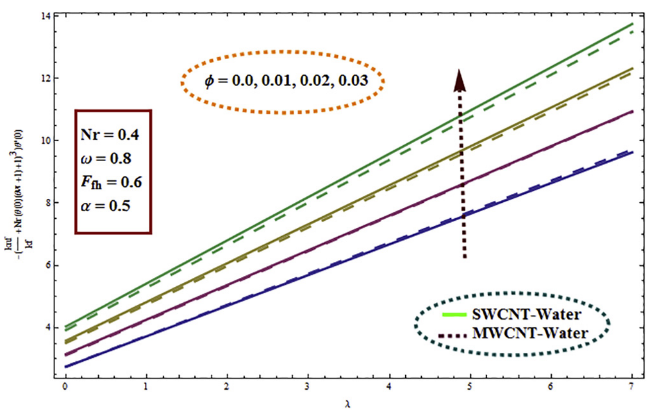

Fig. 19. $Nu\,\mathrm{Re}_x^{-0.5}$ via ϕ and λ.

source ($\lambda > 0$) and heat sink ($\lambda < 0$) variables on temperature ($\theta(\eta)$) are captured in Figs. 11 and 12. Here temperature of liquid rises for larger heat source ($\lambda > 0$) while it decays with heat sink. Fig. 13 presents the impact of nanoparticle volume fraction (ϕ) on ($\theta(\eta)$). An increasing behavior of thermal diffusivity is observed for an increment in nanoparticle volume fraction. Such enhancement in thermal diffusivity provides stronger thermal field. Also stronger thermal layer is noticed for both MWCNTs and SWCNTs. Moreover thermal field is stronger in case of MWCNTs when compared with SWCNTs. From Fig. 14 it is clearly scrutinized that a stronger thermal field is generated by larger estimation of (Nr). Physically more kinetic energy occures in this process. That is why thermal field increases for both single wall carbon nanotubes and multi wall carbon nanotubes. Fig. 15 displays effect of (α) on ($\theta(\eta)$). Here temperature is increased function of (α) for both SWCNTs and MWCNTs. Fig. 16 demonstrates that for larger estimation of (θ_w), thermal field and thickness of layer are enhanced for both SWCNTs and MWCNTs. Moreover thermal field is more in case of MWCNTs than SWCNTs. Figs. 17–19 explains the influence of different physical variables like nanoparticle volume fraction, porosity variable and heat generation absorption variable on surface drag forces (skin friction coefficients) and heat transfer rate (Nusselt number). We observed that surface drag force decays for higher (ϕ) along x-direction while it increases in y-direction (see Figs. 17 and 18). We also noticed that heat transfer rate has larger for nanoparticle volume fraction and porosity. Physically for lager porosity variable the motion of liquid particles faced more resistance. Also internal energy of particle enhances for higher thermal diffusivity which is directly proportional to the nanoparticle volume fraction. Therefore heat transfer rate enhances (see Fig. 19).

Final conclusions

The main points of present flow are:

- Velocity field decays for larger estimations of porosity and ratio of stretching variables.
- Estimations of F_l on velocity and temperature are opposite.
- Velocity components along x and y axies have reverse behavior for nanoparticles volume fraction.
- Temperature increases for an enhancement in volume fraction (ϕ).
- Increasing values of temperature ratio and radiation variables lead to stronger temperature distribution.
- ($Cf_x\,\mathrm{Re}_x^{\frac{1}{2}}$) increases for estimations of (ϕ) and (ω).
- Heat transfer rate is enhanced for larger nanoparticle volume fraction.

References

[1] Choi SUS, Zhang ZG, Yu W, Lockwood FE, Grulke EA. Anomalous thermal conductivity enhancement in nanotube suspensions. AIP Appl Phys Lett 2001;79:2252.
[2] Xue QZ. Model for thermal conductivity of carbon nanotube-based composites. Physica B 2005;368:302–7.
[3] Hayat T, Kiran A, Imtiaz M, Alsaedi A. Unsteady flow of carbon nanotubes with chemical reaction and Cattaneo-Christov heat flux model. Results Phys 2017;7:823–31.
[4] Mahanthesh B, Gireesha BJ, Shashikumar NS, Shehzad SA. Marangoni convective MHD flow of SWCNT and MWCNT nanoliquids due to a disk with solar radiation and irregular heat source. Physica E 2017;94:25–30.
[5] Haq RU, Nadeem S, Khan ZH, Noor NFM. Convective heat transfer in MHD slip flow over a stretching surface in the presence of carbon nanotubes. Physica B 2015;457:40–7.
[6] Hayat T, Khan MI, Farooq M, Alsaedi A, Yasmeen T. Impact of Marangoni convection in the flow of carbon-water nanofluid with thermal radiation. Int J Heat Mass Transfer 2017;106:810–5.
[7] Hayat T, Khan MI, Farooq M, Yasmeen T, Alsaedi A. Water-carbon nanofluid flow with variable heat flux by a thin needle. J Mol Liq 2016;224:786–91.
[8] Hayat T, Khan MI, Waqas M, Alsaedi A, Farooq M. Numerical simulation for melting heat transfer and radiation effects in stagnation point flow of carbon–water nanofluid. Comput Methods Appl Mech Eng 2017;315:1011–24.
[9] Imtiaz M, Hayat T, Alsaedi A, Ahmad B. Convective flow of carbon nanotubes between rotating stretchable disks with thermal radiation effects. Int J Heat Mass Transfer 2016;101:948–57.
[10] Raju CSK, Sandeep N, Babu MJ, Sugunamma V. Dual solutions for threedimensional MHD flow of a nanofluid over a nonlinearly permeable stretching sheet. Alexandria Eng J 2016;55:151–62.
[11] Forchhiemer P. Wasserbewewegung durch Boden. Zeitschrift Ver D Ing 1901;45:1781.
[12] Hayat T, Ahmad S, Khan MI, Alsaedi A. Non-Darcy Forchheimer flow of ferromagnetic second grade fluid. Results Phys 2017;7:3419–24.
[13] Hayat T, Hussain Z, Ahmed B, Alsaedi A. Base fluids with CNTs as nanoparticles through non-Darcy porous medium in convectively heated flow: a comparative study. Adv Powder Technol 2017;28:1855–65.
[14] Hayat T, Shah F, Alsaedi A, Khan MI. Development of homogeneous/heterogeneous reaction in flow based through non-Darcy Forchheimer medium. J Theor Comput Chem 2017;16:1750045.
[15] Shehzad SA, Abbasi FM, Hayat T, Alsaedi A. Cattaneo-Christov heat flux model for Darcy-Forchheimer flow of an Oldroyd-B fluid with variable conductivity and non-linear convection. J Mol Liq 2016;224:274–8.
[16] Gireesha BJ, Mahanthesh B, Manjunatha PT, Gorla RSR. Numerical solution for hydromagnetic boundary layer flow and heat transfer past a stretching surface embedded in non-Darcy porous medium with fluid-particle suspension. J Niger Math Soc 2015;34:267–85.
[17] Khan MI, Hayat T, Alsaedi A. Numerical analysis for Darcy-Forchheimer flow in presence of homogeneous-heterogeneous reactions. Results Phys 2017;7:2644–50.
[18] Sadiq MA, Hayat T. Darcy-Forchheimer flow of magneto Maxwell liquid bounded by convectively heated sheet. Results Phys 2016;6:884–90.
[19] Hayat T, Shah F, Alsaedi A, Hussain Z. Outcome of homogeneous and heterogeneous reactions in Darcy-Forchheimer flow with nonlinear thermal radiation and convective condition. Results Phys 2017;7:2497–505.
[20] Eldabe NT, Abou-zeid MY. Homotopy perturbation method for MHD pulsatile non-Newtonian nanofluid flow with heat transfer through a non-Darcy porous medium. J Egypt Math Soc 2017;25:375–81.
[21] Cortell R. Fluid flow and radiative nonlinear heat transfer over a stretching sheet. J King Saud Univ Sci 2014;26:161–7.

[22] Sheikholeslami M, Ganji DD, Javed MY, Ellahi R. Effect of thermal radiation on magnetohydrodynamics nanofluid flow and heat transfer by means of two phase model. J Magn Magn Mater 2015;374:36–43.
[23] Reddy JVR, Surunamma V, Sandeep N. Impact of nonlinear radiation on 3D magnetohydrodynamic flow of methanol and kerosene based ferrofluids with temperature dependent viscosity. J Mol Liq 2017;236:39–100.
[24] Qayyum S, Khan MI, Hayat T, Alsaedi A. A framework for nonlinear thermal radiation and homogeneous-heterogeneous reactions flow based on silver-water and copper-water nanoparticles: a numerical model for probable error. Results Phys 2017;7:1907–14.
[25] Pal D, Saha P. Influence of nonlinear thermal radiation and variable viscosity on hydromagnetic heat and mass transfer in a thin liquid film over an unsteady stretching surface. Int J Mech Sci 2016;119:208–16.
[26] Khan MI, Waqas M, Hayat T, Alsaedi A, Khan MI. Significance of nonlinear radiation in mixed convection flow of magneto Walter-B nanoliquid. Int J Hydrogen Energy 2017;42:26408–16.
[27] Hayat T, Qayyum S, Alsaedi A, Waqas M. Simultaneous influences of mixed convection and nonlinear thermal radiation in stagnation point flow of Oldroyd-B fluid towards an unsteady convectively heated stretched surface. J Mol Liq 2016;224:811–7.
[28] Khan M, Irfan M, Khan WA. Impact of nonlinear thermal radiation and gyrotactic microorganisms on the Magneto-Burgers nanofluid. Int J Mech Sci 2017;130:375–82.
[29] Hayat T, Tamoor M, Khan MI, Alsaedi A. Numerical simulation for nonlinear radiative flow by convective cylinder. Results Phys 2016;6:1031–5.
[30] Zeeshan A, Majeed A, Ellahi R. Effect of magnetic dipole on viscous ferro-fluid past a stretching surface with thermal radiation. J Mol Liq 2016;215:549–54.
[31] Liao SJ. An optimal homotopy-analysis approach for strongly nonlinear differential equations. Commun Nonlinear Sci Numer Simul 2010;15:2003–16.